Energy & Environmental Science

ROYAL SOCIETY OF CHEMISTRY

PAPER

View Article Online
View Journal | View Issue

Cite this: *Energy Environ. Sci.*, 2025, **18**, 3740

Buried and bulk synergistic engineering enables high-performance inverted 2D/3D perovskite solar cells†

Zonglong Song,‡[a] Yu Zou,‡[a] Yuping Gao,[a] Xingbang Gao,[a] Liu Yang,[d] Hang Liu,[a] Yuting Ma,[a] Rui Wang,[a] Ziyang Hu,[d] Yongsheng Chen,[ab] Baomin Xu*[c] and Yongsheng Liu*[ab]

Received 9th January 2025,
Accepted 4th March 2025

DOI: 10.1039/d5ee00156k

rsc.li/ees

Crystal growth regulation plays a key role in the fabrication of high-quality perovskite films. While surface defects have been extensively studied, the optimization of buried interfaces and bulk properties remains a significant challenge due to their complex influence on film morphology and device performance. Here, a synergistic strategy was developed to improve perovskite film quality by modifying the buried interface with FuMACl and controlling bulk crystallization using $(DFP)_2PbI_4$ 2D perovskite crystal seeds. The FuMACl layer improves the wettability, alleviates residual stress at the buried interface, and passivates defects. Combined with the $(DFP)_2PbI_4$ seeds in bulk, these modifications effectively enhance film quality and increase grain size, leading to a significantly reduced defect density. Compared to the control device with an efficiency of 23.11%, the target device demonstrated a champion efficiency of 26.03% and a notable fill factor of 86.79%, along with improved stability. Moreover, perovskite mini-modules with an aperture area of 10.80 cm^2 achieved 22.89% efficiency. These findings highlight the potential of the synergistic effects of buried interfaces and bulk engineering strategies to significantly enhance the performance of PSCs.

Broader context

2D/3D perovskite solar cells (PSCs) have garnered considerable attention for their potential to combine the high stability of 2D PSCs with the superior efficiency of 3D PSCs. However, a critical challenge remains in overcoming the poor wettability of perovskite precursor solutions on widely used NiO_x/SAM substrates. This issue undermines both the crystal quality at the buried interface and the bulk properties of the perovskite film, limiting the overall performance of the devices. Addressing the dual problem of optimizing the buried interface to enhance wettability and reduce defects, while simultaneously improving the bulk crystallization process to ensure high-quality films, is essential for advancing PSC technology. In this work, we developed an effective strategy to improve the efficiency and stability of inverted PSCs through the synergistic optimization of the buried interface using furan-2-ylmethanaminium chloride (FuMACl) and bulk properties using $(DFP)_2PbI_4$ crystal seeds. The resulting perovskite film exhibited alleviated residual stress, enlarged grain size and significantly reduced grain boundaries. Consequently, the optimized device achieved a champion PCE of 26.03% and an impressive fill factor of 86.79%. This work highlights the potential of the synergistic effects of buried interfaces and bulk engineering strategies to significantly enhance the performance of PSCs.

1. Introduction

Metal halide perovskites have attracted substantial interest from both the scientific community and investors due to their rapidly advancing photovoltaic efficiency and promising application potential in sustainable energy systems.[1–4] The development of perovskite photovoltaic technology holds significant potential to address the urgent global energy and environmental crises.[5–7] Despite notable progress, perovskite solar cells (PSCs) still face critical challenges related to device performance and stability.[8–10] Enhancing these aspects requires precise control of the interface between the perovskite absorption

[a] *The Centre of Nanoscale Science Technology, Key Laboratory of Functional Polymer Materials (Ministry of Education), Frontiers Science Center for New Organic Matter (Ministry of Education), College of Chemistry, Nankai University, Tianjin 300071, China. E-mail: liuys@nankai.edu.cn*
[b] *Haihe Laboratory of Sustainable Chemical Transformations, Tianjin 300192, China*
[c] *Department of Materials Science and Engineering, SUSTech Energy Institute for Carbon Neutrality, Southern University of Science and Technology, Shenzhen 518055, China. E-mail: xubm@sustech.edu.cn*
[d] *Department of Microelectronic Science and Engineering, School of Physical Science and Technology, Ningbo University, Ningbo 315211, China*

† Electronic supplementary information (ESI) available. See DOI: https://doi.org/10.1039/d5ee00156k

‡ These authors contributed equally to this work.

layer and the charge transport layer.[11–14] It is well known that obtaining high-quality perovskite films is crucial for addressing the aforementioned issues.[15,16] However, perovskite films often exhibit numerous defects that degrade both photovoltaic efficiency and stability, with defects predominantly distributed on the top and bottom surfaces of the perovskite films. This makes effective modulation of the perovskite surface crucial to advancing device performance.[17] Compared to the buried interface, the exposed surface of perovskite films is more readily controllable. As a result, surface post-treatments, including surface modification and surface energy level regulation, have become prominent areas of research in recent years.[17–20] Although optimizing the buried interface is equally important, the inherent difficulty of direct observation and characterization leaves many fundamental questions unresolved.[21,22]

2D/3D PSCs have been extensively employed to combine the high stability of 2D PSCs with the superior efficiency of 3D PSCs.[23–29] Wolf *et al.* introduced a method to minimize the dissolution of 2D ligands during perovskite solution casting, thereby strengthening their interaction with the substrate and resulting in the formation of a 2D perovskite layer underneath the 3D perovskite film.[30] Hou *et al.* developed a ligand-mediated surface passivation strategy to create a phase-pure 2D perovskite passivation layer on top of the 3D perovskite film, achieving a homogeneous energy landscape through dual-ligand co-deposition.[31] Zang *et al.* proposed a strategy to control the crystallization of methylammonium-free perovskite by incorporating a small amount of 2-aminoindan hydrochloride into the precursor inks, leading to the formation of a bottom-up 2D/3D heterojunction.[32] In inverted p–i–n 2D/3D PSCs, the perovskite layer is deposited on the hole transport layer (HTL). The top interface of the HTL plays an important role in perovskite nucleation and heterojunction formation.[33,34] As an efficient interface layer, self-assembled monolayers (SAMs) have significantly boosted the efficiency of inverted PSCs due to their high hole selectivity, efficient hole transport, and the potential to reduce trap density in perovskite films.[11] For example, Wu *et al.* reported an amphiphilic molecule, (2-(4-(bis(4-methoxyphenyl) amino) phenyl)-1-cyanovinyl) phosphonic acid, for the HTL and achieved a certified power conversion efficiency (PCE) of 25.4%.[13] Hou *et al.* demonstrated that the amorphous phases of SAMs can realize a more homogeneous perovskite growth, achieving a PCE of 25.20%.[35] However, the poor wettability of the perovskite precursor solution on top of the NiO_x/SAM substrate could negatively impact both the crystal quality at the buried interface and bulk properties of the perovskite film. As a result, optimizing the buried interface to enhance wettability and reduce defects, along with improving the bulk crystallization process to ensure high film quality, remains a pressing challenge for advancing PSC technology.

In this work, we developed an effective strategy to improve the efficiency and stability of inverted PSCs through the synergistic optimization of the buried interface using furan-2-ylmethanaminium chloride (FuMACl) and bulk properties using $(DFP)_2PbI_4$ crystal seeds. It is found that the FuMACl can improve the wettability of perovskite precursor solution and reduce buried defects. Combined with the advantages of incorporating 2D perovskite seeds, the obtained perovskite film exhibits alleviated residual stress, enlarged grain size and significantly reduced grain boundaries. As a result, the optimized device achieved a champion PCE of 26.03% for a 0.1 cm^2 device and 22.89% for a minimodule (5 cm × 5 cm), accompanied by a notable improvement in device stability. Additionally, when applied to wide-bandgap perovskites (E_g = 1.80 eV), the methodology achieved a PCE of 18.88% and a high V_{oc} of 1.345 V.

2. Results and discussion

The fabrication process of the perovskite film is illustrated in Fig. 1a. The chemical structures of FuMA and DFP spacers are shown in Fig. S1 (ESI†), with specific synthesis of FuMACl following procedures reported in our previous work.[36] For clarity, the device incorporating FuMACl at the buried interface between the perovskite and HTL is referred to as target-1. Building upon this, we incorporated $(DFP)PbI_4$ 2D perovskite single crystals into the perovskite precursor solution, and the corresponding device was named target-2. The $(DFP)_2PbI_4$ 2D perovskite crystal seeds were selected for their ability to passivate Pb^{2+} defects and act as nucleation sites, which enhance perovskite crystallization as discussed below.[18,21] Fourier transform infrared spectroscopy (FTIR) (Fig. S2, ESI†) analysis revealed no obvious chemical interaction between FuMACl and NiO_x/SAM. However, the hydrophilic amino groups in FuMACl improved the wettability and reduced defects, which was also confirmed by better photovoltaic performance when FuMACl was applied to other HTLs like PTAA and 2PACZ (Table S1, ESI†). To investigate the interaction between FuMACl and PbI_2, we conducted Fourier transform infrared spectroscopy (FTIR) on mixed powders of PbI_2 and FuMACl. Peaks located at around 1243 cm^{-1} and 1064 cm^{-1} correspond to the asymmetric stretching vibration (ν_{as}) and the symmetric stretching vibration (ν_s) of the C–O–C group, respectively (Fig. 1b). The shifts in these characteristic peaks likely resulted from the $Pb^{2+}\cdots O$ interactions between FuMACl and PbI_2. To further investigate the interaction between FuMACl and PbI_2, we conducted proton nuclear magnetic resonance (^1H NMR) on the solution containing FuMACl and PbI_2. As shown in Fig. 1c, the chemical shift of the H atom adjacent to the O atom in the furan ring moved upfield, supporting the coordination interaction between the O atom in FuMACl and Pb^{2+}. ^1H NMR in Fig. S3 (ESI†) shows a downfield shift of the NH_3^+ group on the FuMACl, primarily attributed to the hydrogen bonding interaction between the NH_3^+ group and I- ions. This interaction enhances electron density, increasing the shielding effect.[37]

X-ray photoelectron spectroscopy (XPS) measurements were performed to examine the chemical states of surface elements in perovskite films. In Fig. 1d, the control perovskite film exhibits two primary I 3d peaks at 618.56 eV (I $3d_{7/2}$) and 630.03 eV (I $3d_{3/2}$). In the target-1 and target-2 films, the I $3d_{5/2}$ peaks appear at 618.88 and 618.73 eV, respectively. Compared to the control sample, the I 3d peaks in target-1 and target-2 films initially shift toward higher binding energy and then towards lower binding energy. A similar trend is

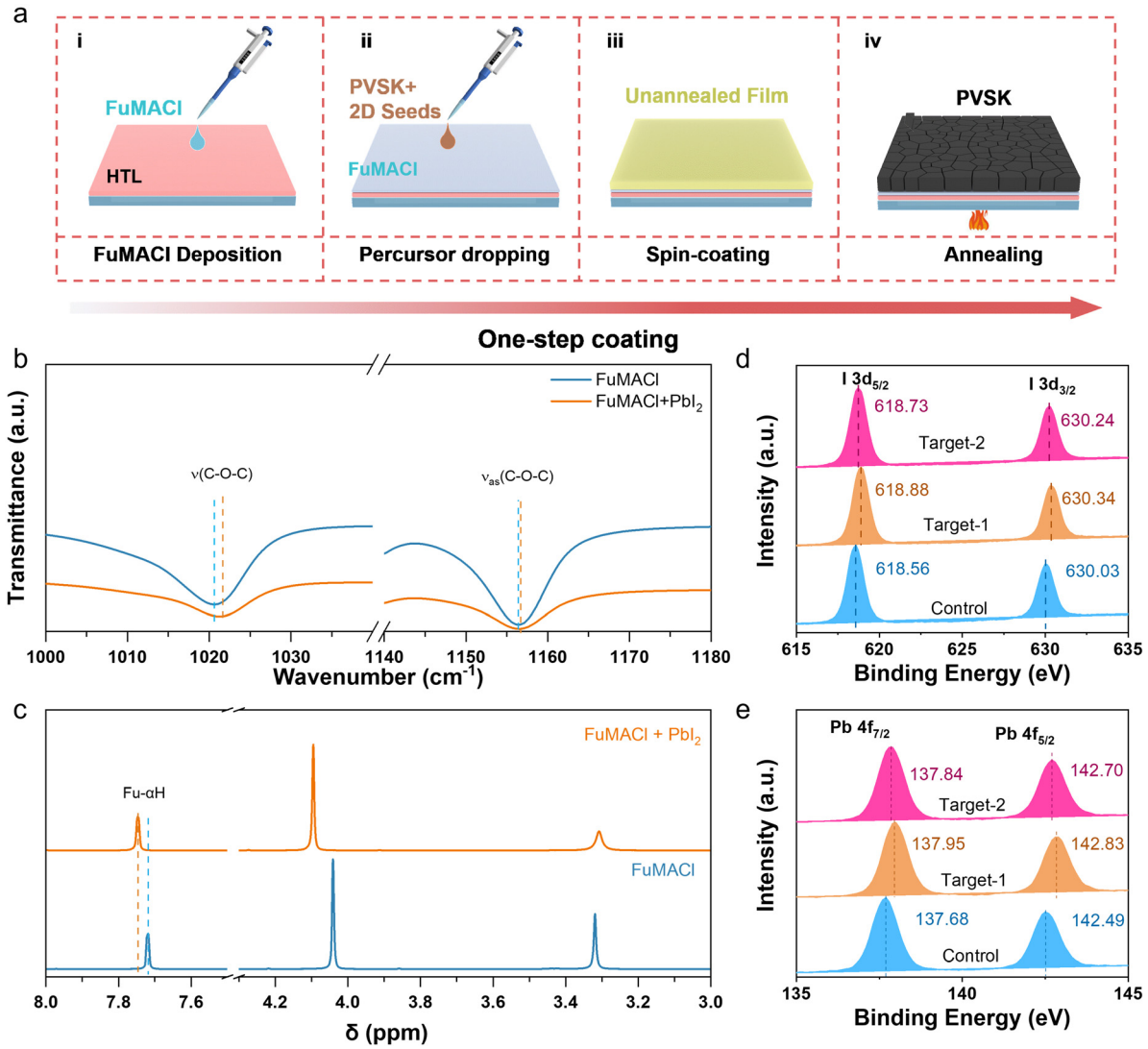

Fig. 1 (a) Process diagram of the one-step spin-coating method for preparing target perovskite films. (b) FTIR spectra of FuMACl and FuMACl/PbI_2 complex. (c) Chemical shift information of FuMACl and FuMACl/PbI_2 complex obtained from ^{1}H NMR measurements. (d) and (e) XPS spectra of the control, target-1 and target-2 perovskite films.

observed in the binding energy shifts of Pb 4f and N 1s peaks (Fig. 1e and Fig. S4, ESI†). These findings indicate that the incorporation of the FuMACl interface layer and DFPI single crystal seeds alters the chemical environment of Pb^{2+} and I^- in the perovskite films.

To investigate the influence of FuMACl on the buried interface of the perovskite film, we employed a UV-curable adhesive delamination method to expose the buried interface and examine morphology changes (Fig. 2a). The specific procedure is as follows: first, a layer of UV-curable adhesive was uniformly coated on the surface of a glass substrate. Next, the adhesive-coated glass was gently placed onto the perovskite film and exposed to UV light for 20 minutes to ensure tight adhesion between the glass substrate and perovskite. Finally, the glass substrate was separated from the ITO and HTL-covered substrate, effectively transferring the perovskite layer onto the glass. Scanning electron microscope (SEM) analysis was conducted on the delaminated film to evaluate the crystallinity at the perovskite buried interface. As shown in Fig. 2b–d, the control film exhibited numerous amorphous regions at the buried interface, with small grains and many pinholes. After introducing a FuMACl layer before the deposition of perovskite, there was a significant enhancement in the crystalline quality, characterized by well-formed perovskite grains. In the target-2 film, the perovskite grains at the buried interface were even larger, indicating further improvement in crystallinity with the addition of $(DFP)_2PbI_4$ seeds. The results indicate that the incorporation of organic spacers at the buried interface and/or perovskite bulk can promote the crystallization of the perovskite film, aiding in defect reduction.

To investigate the effect of FuMACl on the wettability of the substrates, we conducted contact angle tests on Me-4PACz-coated ITO/NiO_x with and without FuMACl modification of the Me-4PACz layer. As shown in Fig. S5a and b (ESI†), the contact angle of the mixed solution of DMF and DMSO on the

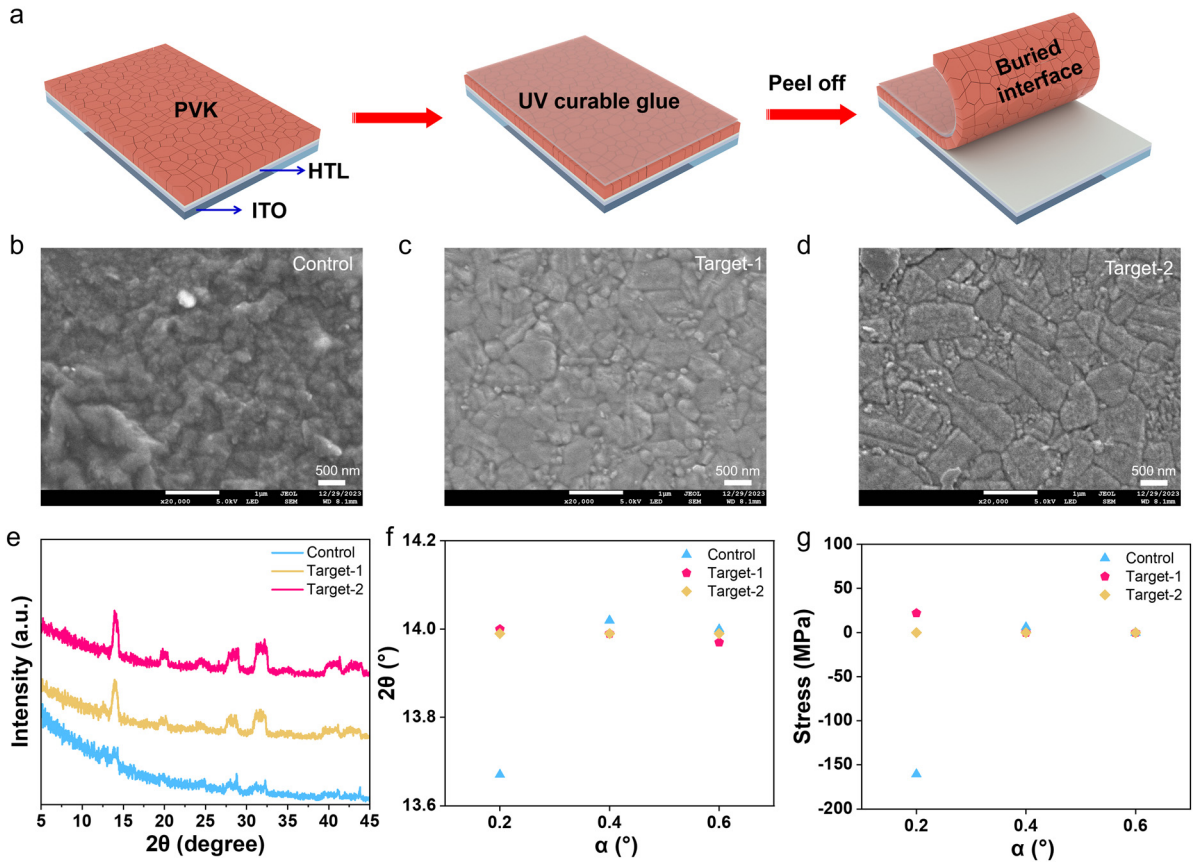

Fig. 2 (a) Illustration of buried interface delamination in perovskite. (b) Buried interface SEM images of the control film. (c) Buried interface SEM images of the target-1 film. (d) Buried interface SEM images of the target-2 film. (e) GIXRD results performed on the exposed buried interface of the control, target-1 and target-2 films with an incidence angle (α) of 0.1°. (f, g) Diffraction angle and stress from GIXRD tests of the control, target-1 and target-2 films at different incidence angles.

buried interface decreased from 62.20° to 25.95° upon introducing FuMACl, suggesting enhanced wettability of the perovskite precursor on SAMs. However, the presence of FuMACl at the buried interface does not preclude the possibility of partial or complete dissolution and reintegration of FuMACl into the 3D perovskite bulk during spin-coating of the perovskite precursor. XPS analysis of ITO/NiO_x/SAM/FuMACl before and after washing with DMF/DMSO (4 : 1, v/v) (Fig. S5c, ESI†) showed a significant reduction in the Cl 2p peak, indicating that some FuMACl has been washed off, but a portion remains at the interface, suggesting that FuMACl continues to be effective despite some dissolution. To verify the presence of the FuMACl-based 2D perovskite in the perovskite film, we performed high resolution-transmission electronic microscope (HRTEM) tests on control and target-1 films (Fig. S6, ESI†). The HRTEM image of the control film exhibits a lattice spacing of 3.1 Å, corresponding to 3D perovskite, whereas the target-1 film exhibits a lattice spacing of 7.4 Å, corresponding to the diffraction of the (004) plane for the 2D RP perovskite (n = 1) phase.[36] This finding suggests the formation of 2D/3D structures in target-1 perovskite films.

Grazing incidence X-ray diffraction (GIXRD) at different incident angles was performed to examine the effect of FuMACl and $(DFP)_2PbI_4$ seeds on crystallinity and residual stress at the buried interface. At an incident angle of 0.1° (approximate detection depth of 30 nm), the crystallinity of the exposed buried interface was analyzed. The control film exhibited poor crystallinity with a weak (110) diffraction peak (Fig. 2e). In contrast, target-1 and target-2 films exhibited much stronger diffraction signals at the buried interface, indicating substantial crystallinity improvement. To further investigate residual stress, we examined shifts in the (110) crystal plane at different incident angles. As shown in Fig. S7 (ESI†), the control perovskite film exhibited substantial angular shifts, while target-1 and target-2 films showed minimal deviation, suggesting that FuMACl effectively eliminated stress/strain at the buried perovskite interface.[38] The residual stress was calculated by analyzing the displacement of the (110) crystal plane at different angles (Fig. 2f and g).[39,40] The residual stress primarily arises at the buried interface due to thermal expansion and contraction during the annealing process of the HTL and the perovskite layer. The significant difference in thermal expansion coefficients between these layers leads to stress in the perovskite film.[41] Elevated residual stress can induce severe lattice distortion, creating defects and traps at the interface.[21] The reduction of residual stress in the target-1 and target-2 films thus enhances both the photovoltaic performance and stability of PSCs as discussed below.

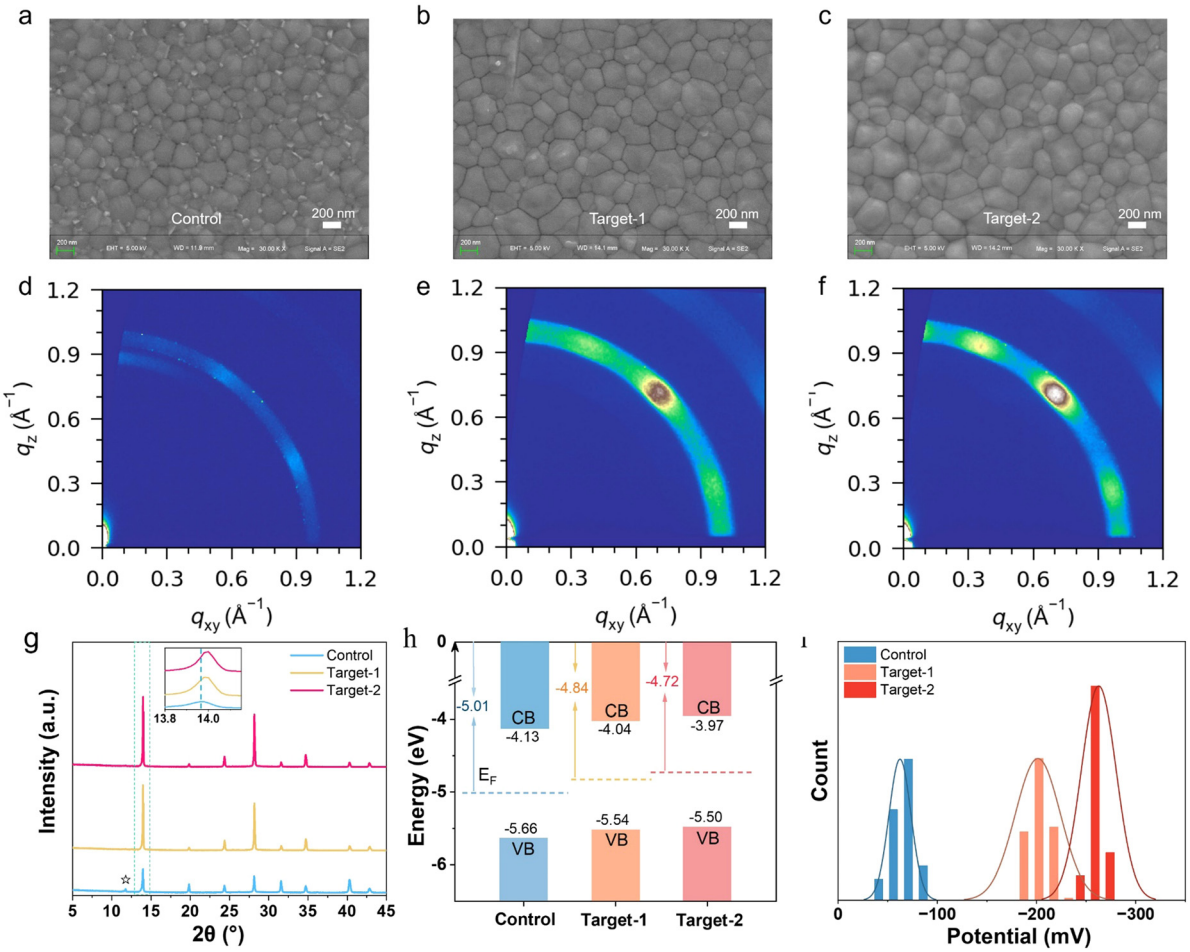

Fig. 3 (a) Top-view SEM image of the control film. (b) Top-view SEM image of the target-1 film. (c) Top-view SEM image of the target-2 film. (d)–(f) GIWAXS patterns of the control, target-1 and target-2 films. (g) XRD patterns of the control, target-1 and target-2 perovskite films. (h) Energy-level diagrams of the perovskite films. (i) KPFM of the control, target-1 and target-2 perovskite films.

To further investigate the influence of the 2D RP perovskite $(DFP)_2PbI_4$ seed crystals on the film morphology, dynamic light scattering (DLS) measurement was conducted on the respective precursor solutions. As shown in Fig. S8 (ESI†), the control perovskite solution exhibited an aggregate size smaller than 500 nm, while the aggregate size in the target-2 perovskite precursor solution was increased to ~1.5 μm. Note that the perovskite precursor doped only with DFPI salt displayed an aggregate size between that of the control and target-2 solutions. Larger precursor clusters promote the reduction of Gibbs free energy during perovskite nucleation, ultimately leading to increased perovskite grains and improved film quality.[42–44] The SEM images in Fig. 3a–c reveal that the average grain size of the target-1 perovskite film is about 200–400 nm, which is larger than the crystal size of the control 3D perovskite film (100–300 nm) (Fig. S9, ESI†). Upon the incorporation of $(DFP)_2PbI_4$ seed crystals, the average grain size in the target-2 film further increases to 300–500 nm. The improved film quality with enlarged grain sizes reduces the grain boundaries, resulting in decreased defects. Note that the surface of the control perovskite film exhibits obvious white crystals (PbI_2), which are absent on the surfaces of both target-1 and target-2 films. Excess PbI_2 at the perovskite interface is known to detrimentally affect the long-term stability of PSCs.[45] Shown at the bottom of Fig. S10 (ESI†), the cross-sectional SEM images of target-1 and target-2 films reveal vertically oriented crystals with fewer grain boundaries compared to the control film, resulting in a lower defect density as discussed below. Atomic force microscopy (AFM) measurements further confirm the enhanced film quality in the target-1 and target-2 films (Fig. S11, ESI†). The root means square roughness decreases from 30.34 nm for the control film to 28.02 nm for the target-1 film and 23.61 nm for the target-2 film. The reduction in roughness is beneficial for reducing light scattering and enhancing the photocurrent in PSCs.

GIWAXS was employed to characterize changes in the crystallinity of perovskite films following the incorporation of the FuMACl layer and $(DFP)_2PbI_4$ seed crystals. As shown in Fig. 3d–f, compared to the control film, the (110) diffraction peak of the target-1 and target-2 films exhibited increased intensity, and the diffraction pattern evolved from rings to distinct spots, indicating a marked improvement in the

crystallinity of the film. X-ray diffraction (XRD) patterns in Fig. 3g showed that the main diffraction peaks for the target-1 film appear at 13.97° and 28.20°, corresponding to the (110) and (220) crystal planes, respectively. The full width at half maximum (FWHM) values for the (110) peak of the target-1 and target-2 films are 0.109° and 0.103°, respectively, both of which are narrower than that of the control film (FWHM = 0.158°). The reduced FWHM values and increased intensity for the target-1 and target-2 films in comparison with the control film indicate enhanced crystallinity, consistent with the SEM results discussed above.

The energy level diagram of the different perovskite films is shown in Fig. 3h and Fig. S12 (ESI†). Compared to control and target-1 films, the wider energy gap between the Fermi level (E_F) and the valence band maximum (VBM) in the target-2 film indicates enhanced n-type characteristics, which facilitate efficient charge transport.[46] This enhancement can be attributed to the changed components and improved film quality due to the incorporation of the FuMACl layer and 2D seed crystals. Kelvin probe force microscopy (KPFM) measurements were used to measure the surface potential. The images display a more uniform morphology in the target-1 and target-2 films compared to the control film (Fig. S13, ESI†). As illustrated in Fig. 3i, compared to the control film (−40 to −90 mV), a decreased potential from −184 to −235 mV for the target-1 film and −240 to −280 mV for the target-2 film can be observed. The decreased surface potential implies that the Fermi level (E_F) is closer to the valence band maximum (VBM), consistent with the energy level diagram in Fig. 3h.

Fig. 4a and b presents the *J*–*V* curves, while the corresponding photovoltaic data is summarized in Table S2 (ESI†). The control device exhibits a PCE of 23.82%, with a short-circuit current density (J_{sc}) of 24.62 mA cm^{-2}, an open-circuit voltage (V_{oc}) of 1.140 V, and a fill factor (FF) of 84.85%. The PCE of the target-1 device increases to 24.82%, primarily attributed to the improvement in the quality of the perovskite film, the release of residual stress, and a reduction in non-radiative recombination losses. Building upon this, the incorporation of $(DFP)_2PbI_4$ seed crystals into the perovskite bulk phase further elevates the PCE to 26.03%, with a J_{sc} of 25.16 mA cm^{-2}, a high V_{oc} of 1.192 V, and a very notable FF of 86.79%. The high FF of 86.79% could be attributed to the enhancement of the perovskite crystalline quality and the reduction of interface defects through the incorporation of FuMACl and $(DFP)_2PbI_4$, which improve charge transport and minimize non-radiative recombination. The distribution of FF across devices shows an average FF exceeding 85% (Fig. S14 and Table S2, ESI†), demonstrating excellent reproducibility and consistent device performance. The enhancement in V_{oc} (Fig. 4c) for the target-1 and target-2 devices was further validated by characterizing the capacitance–voltage (*C*–*V*) using the Mott–Schottky relationship (Fig. 4d). The V_{bi} values for the control, target-1, and target-2 devices were measured to be 0.86 V, 0.89 V, and 0.93 V, respectively, aligning with the observed increase in V_{oc} from the *J*–*V* curves. The elevation of V_{bi} indicates a greater driving force for charge transfer and collection, thereby facilitating the improvement in V_{oc} for both target-1 and target-2 devices.[47,48] The PCEs of these devices were further verified by the steady-state power output measurements by holding the voltage at the max power point for 120 seconds (Fig. S15, ESI†). The control device achieved an average steady-state PCE of 22.45%, while the target-1 and target-2 devices exhibited average steady-state PCEs of 24.16% and 25.65%, respectively, which are in good agreement with the *J*–*V* data.

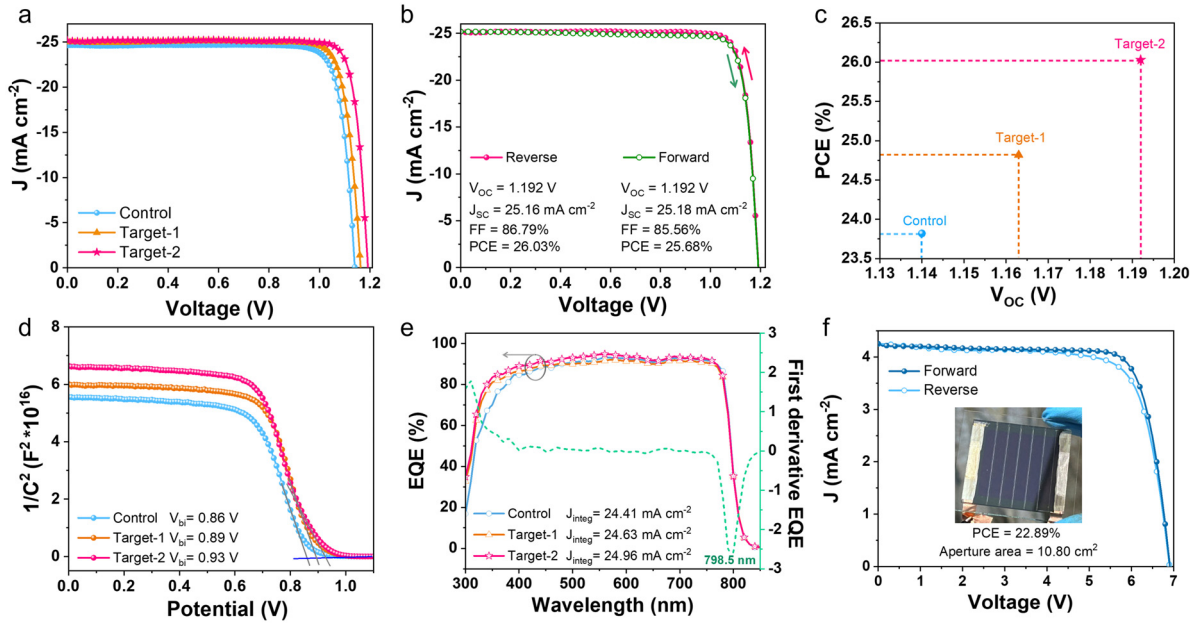

Fig. 4 (a) *J*–*V* curves of the control, target-1 and target-2 devices under reverse scan. (b) *J*–*V* curves of reverse and forward scans for the optimized target-2 device. (c) PCE and V_{oc} of the control, target-1 and target-2 devices. (d) Mott–Schottky plots for the corresponding devices. (e) EQE spectra of the corresponding devices. (f) *J*–*V* curves of reverse and forward scans for the target-2 film based mini-module (10.80 cm^2).

The integrated current densities derived from the external quantum efficiency (EQE, Fig. 4e) are 24.41 mA cm^{-2}, 24.63 mA cm^{-2} and 24.96 mA cm^{-2} for the control, target-1 and target-2 devices, respectively, consistent with the *J–V* results. Note that due to the low concentration of FuMACl, directly measuring its thickness is challenging. However, we optimized the device performance by spin-coating FuMACl on NiOx/SAM surfaces at different concentrations (Table S3, ESI†).

The light intensity dependence of V_{oc} (Fig. S16, ESI†) for the control device shows a slope of 1.98 $kT\,q^{-1}$, where q represents the charge, k is the Boltzmann constant, and T means the absolute temperature.[49] In contrast, the slopes for the target-1 (1.68 $kT\,q^{-1}$) and target-2 (1.53 $kT\,q^{-1}$) devices are much lower, suggesting that the reduction of defect density in the optimized perovskite films inhibits defect-assisted non-radiative recombination under open-circuit conditions. Additionally, this synergistic method was used to fabricate mini-modules (5 cm × 5 cm) comprising six sub-cells for each module with an aperture area of 10.80 cm^2. The optimized series-connected module shows a V_{oc} of 6.91 V, a J_{sc} of 4.25 mA cm^{-2}, and an FF of 78.17%, achieving a PCE of 22.89% (Fig. 4f and Table S4, ESI†).

The impact of FuMACl and 2D $(DFP)_2PbI_4$ seed crystals on the carrier lifetime of perovskite films was elucidated using steady-state photoluminescence (PL) and time-resolved photoluminescence decay (TRPL) measurements, with perovskite films fabricated on the ITO/NiO_x/Me-4PCACz substrates. As shown in Fig. 5a, the PL intensity of the target-1 film was decreased due to the incorporation of FuMACl at the buried interface. Moreover, the PL intensity of the target-2 film decreased even further, indicating that FuMACl reduced non-radiative recombination at the buried interface, thereby accelerating carrier extraction. TRPL measurements (Fig. 5b) revealed that the carrier extraction rate for the control film was slower, with a long decay time constant of 553 ns, while the decay time constant for the target-1 film shortened to 92 ns, indicating a significant reduction in interface defects and faster carrier extraction in the FuMACl treated perovskite film. The carrier extraction rate of the target-2 films was further shortened to 36 ns, indicating that $(DFP)_2PbI_4$ crystal seed-induced crystallization reduced bulk perovskite defects and further suppressed non-radiative recombination. PL tests on the stripped perovskite buried interface (Fig. S17, ESI†) showed that the target-2 film exhibited the strongest PL intensity. These results indicate that the synergistic effect of seed-induced crystal growth and buried interface defect passivation thus contributed to a reduction in both buried interface and internal defects, leading to reduced non-radiative recombination loss.

To evaluate the carrier dynamics under operating conditions, we performed transient photovoltage decay (TPV) and transient photocurrent decay (TPC) measurements. As shown in Fig. S18a (ESI†), the charge recombination time constant (τ) for the target-2 device is 485 μs, which decreased to 263 μs for the target-1 device and 71 μs for the control device. The improved carrier lifetime in the target-2 device suggests its reduced non-radiative recombination. The TPC curves (Fig. S18b, ESI†) further revealed that the decay time for the target-2 device is 15.9 ns, which is shorter than that of the control device (τ = 17.9 μs), indicating improved charge collection efficiency.

The defect density (N_t) was obtained using the space charge limited current (SCLC) method under dark conditions. As shown in Fig. 5c, the electron defect density calculated from the SCLC data decreases from 7.45 × 10^{16} cm^{-3} in the control film to 4.13 × 10^{16} cm^{-3} and 2.65 × 10^{16} cm^{-3} in the target-1

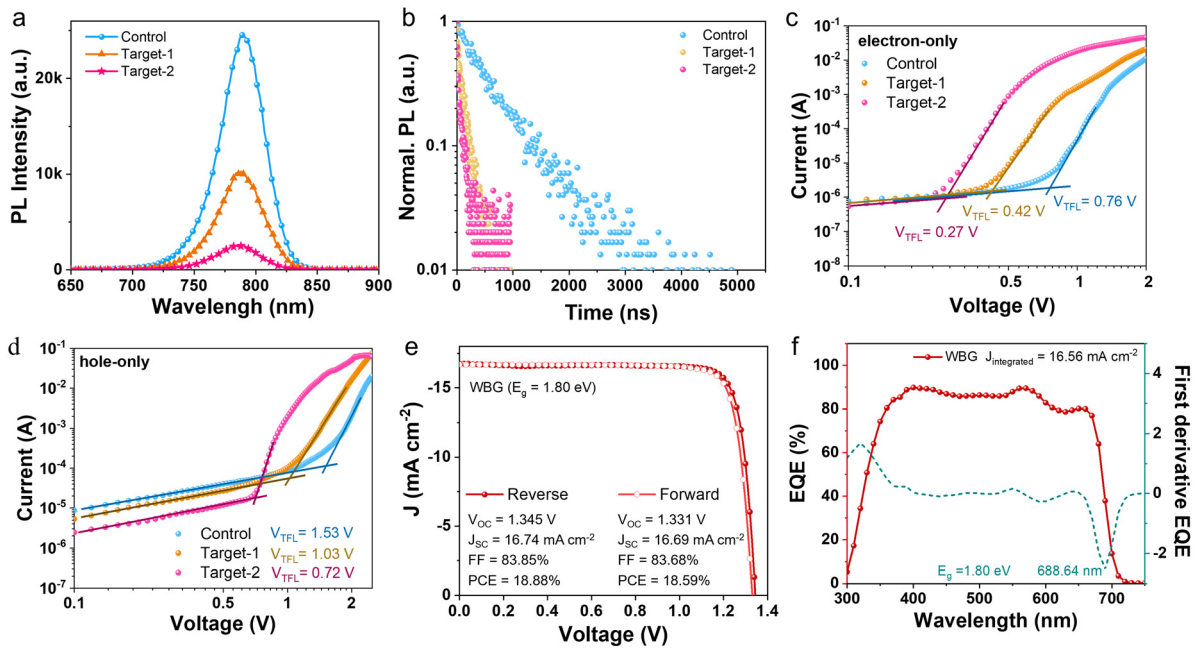

Fig. 5 (a) Steady-state PL of the control, target-1 and target-2 perovskite films. (b) TRPL spectra of the corresponding perovskite films. (c) and (d) Carrier trap density comparison of electron-only (h) and hole-only (i) devices based on the control, target-1 and target-2 films. (e) *J–V* curves of the WBG PSCs with an E_g of 1.80 eV. (f) EQE spectra of the WBG target device.

and target-2 films, respectively. A similar trend can be observed for the hole defect density in Fig. 5d, which decreases from 1.50×10^{17} cm^{-3} in the control film to 1.01×10^{17} cm^{-3} in the target-1 film and 7.07×10^{16} cm^{-3} in the target-2 film. These results further verified that the synergistic effects of FuMACl-assisted defect passivation and seed-induced crystal growth effectively reduce the buried interface and internal defects in perovskite films.

To validate the universality of the synergistic method, we applied this approach to a wide-bandgap (WBG) perovskite with an E_g of 1.80 eV (Fig. 5e) and the detailed data is summarized in Table S5 (ESI†). The PCE of the WBG perovskite device increased significantly from 15.47% to 18.88%, with V_{oc} increasing from 1.241 V to 1.345 V, and the FF increased from 73.34% to 83.85%. The integrated current density obtained from the EQE in Fig. 5f is 16.56 mA cm^{-2} for the WBG target device, consistent with the *J–V* results. The successful application of this strategy in WBG PSCs highlights the universality and broad applicability of buried interface optimization and 2D perovskite crystal seed assisted crystal growth for high-performance PSCs.

The aging test results for non-encapsulated devices stored in ambient air (RH, 45% ± 5%) are shown in Fig. S19 and S20 (ESI†). After 2500 hours, the target-1 and target-2 devices retained 91% and 92% of their original PCE, respectively, whereas the control device decreased to 82% of its initial efficiency after 1000 hours. The thermal aging test results at 60 °C are presented in Fig. S21 and S22 (ESI†). The target-1 device retained 88% of its original efficiency after 1200 hours and the target-2 device retained 91% of its initial PCE after 1872 hours, whereas the control device degraded to 79% of its initial PCE after 400 hours. The long-term stability of encapsulated PSCs was tracked at MPP under a white LED (100 mW cm^{-2}) in a N_2-filled glovebox (T = 45 °C) (Fig. S23, ESI†). The T_{80} lifetime of the target-2 device is 1150 hours, whereas the T_{80} lifetime of control and target-1 devices decreased to 400 hours and 760 hours, respectively. The improved device stability could be attributed to the synergistic effects of seed-induced growth and buried interface defect passivation, which eliminate stress/strain at the buried interface, reduce interface defects, and enhance the quality of the perovskite film.

3. Conclusion

In conclusion, we successfully developed an effective strategy to enhance the efficiency and stability of inverted PSCs by synergistic engineering optimization of the buried interface and bulk properties of the perovskite film. We found that the incorporation of FuMACl at the buried interface improved the wettability, facilitated larger grain formation, passivated defects and alleviated stress/strain although it can easily be washed away by solvents, suggesting that it may not be necessary for this modified layer to remain at the bottom after the perovskite film deposition. The 2D $(DFP)_2PbI_4$ seed crystals incorporated into the perovskite precursor further improved the film quality and reduced defects. These advancements resulted in a very notable FF of 86.79% and a remarkable PCE of 26.03% for the target-2 device, compared to a PCE of 24.82% for the target-1 device and 23.82% for the control device. Importantly, this method also enabled the fabrication of a high-performance perovskite minimodule (aperture area, 10.8 cm^2), achieving a PCE of 22.89%. This synergistic strategy further demonstrated applicability in WBG (E_g = 1.80 eV) PSCs, raising the PCE from 15.47% to 18.88%. Importantly, the stability of the target-2 perovskite device was notably enhanced. The buried and bulk synergistic strategy for the fabrication of high-quality perovskite films provides a scalable approach to improve the performance of inverted PSCs.

Author contributions

Y. L. conceived the idea and designed the research. Z. S. performed the small-area solar cell fabrication and carried out all the performance studies. Y. Z. performed the minimodule fabrication and characterization. Y. G. and X. G. partly supported the fabrication and characterization of perovskite devices. L. Y. and Z. H. contributed to the KPFM measurements. Y. M. performed the GIWAXS measurements. H. L. and R. W. supported the material synthesis of organic salts. Y. C. supported the guidance of the project. B. X. and Y. L. supervised the entire project. All authors discussed the results and reviewed the manuscript.

Data availability

The data supporting this article have been included in this article or as part of the ESI.†

Conflicts of interest

The authors declare no competing financial interest.

Acknowledgements

The authors gratefully acknowledge the financial support from National Key Research and Development Program of China (Grant No. 2024YFB4205201) and the National Natural Science Foundation of China (Grants No. 22479121, 52273182).

References

1 H. Chen, C. Liu, J. Xu, A. Maxwell, W. Zhou, Y. Yang, Q. L. Zhou, A. S. R. Bati, H. Y. Wan, Z. W. Wang, L. W. Zeng, J. K. Wang, P. Serles, Y. Liu, S. Teale, Y. J. Liu, M. I. Saidaminov, M. Z. Li, N. Rolston, S. Hoogland, T. Filleter, M. G. Kanatzidis, B. Chen, Z. J. Ning and E. H. Sargent, *Science*, 2024, **384**, 189–193.
2 A. K. Jena, A. Kulkarni and T. Miyasaka, *Chem. Rev.*, 2019, **119**, 3036–3103.

3 A. Kojima, K. Teshima, Y. Shirai and T. Miyasaka, *J. Am. Chem. Soc.*, 2009, **131**, 6050–6051.
4 J. Y. Shao, D. M. Li, J. J. Shi, C. Ma, Y. S. Wang, X. M. Liu, X. Y. Jiang, M. M. Hao, L. Z. Zhang, C. Liu, Y. T. Jiang, Z. H. Wang, Y. W. Zhong, S. F. Liu, Y. H. Mai, Y. S. Liu, Y. X. Zhao, Z. J. Ning, L. Z. Wang, B. M. Xu, L. Meng, Z. Q. Bian, Z. Y. Ge, X. W. Zhan, J. B. You, Y. F. Li and Q. B. Meng, *Sci. China: Chem.*, 2023, **66**, 10–64.
5 C. Yang, W. J. Hu, J. L. Liu, C. Z. Han, Q. J. Gao, A. Y. Mei, Y. H. Zhou, F. W. Guo and H. W. Han, *Light:Sci. Appl.*, 2024, **13**, 227.
6 N. G. Park and K. Zhu, *Nat. Rev. Mater.*, 2020, **5**, 333–350.
7 L. X. Zhang, H. Li, K. Zhang, W. Z. Li, C. T. Zuo, G. O. Odunmbaku, J. D. Chen, C. Chen, L. Z. Zhang, R. Li, Y. P. Gao, B. M. Xu, J. Z. Chen, Y. S. Liu, Y. Wang, Y. L. Song, J. X. Tang, F. Gao, Q. Zhao, Y. Peng, M. Z. Liu, L. Tao, Y. L. Li, Z. M. Fang, M. Cheng, K. Sun, D. W. Zhao, Y. X. Zhao, S. H. Yang, C. Y. Yi and L. M. Ding, *iEnergy*, 2023, **2**, 172–199.
8 H. W. Zhu, S. Teale, M. N. Lintangpradipto, S. Mahesh, B. Chen, M. D. McGehee, E. H. Sargent and O. M. Bakr, *Nat. Rev. Mater.*, 2023, **8**, 569–586.
9 Q. Jiang, R. Tirawat, R. A. Kerner, E. A. Gaulding, Y. M. Xian, X. M. Wang, J. M. Newkirk, Y. F. Yan, J. J. Berry and K. Zhu, *Nature*, 2023, **623**, 313–318.
10 Y. Bai, Z. J. Huang, X. Zhang, J. Z. Lu, X. X. Niu, Z. W. He, C. Zhu, M. Q. Xiao, Q. Z. Song, X. Y. Wei, C. Y. Wang, Z. H. Cui, J. Dou, Y. H. Chen, F. T. Pei, H. C. Zai, W. Wang, T. L. Song, P. F. An, J. Zhang, J. C. Dong, Y. M. Li, J. J. Shi, H. B. Jin, P. W. Chen, Y. C. Sun, Y. J. Li, H. N. Chen, Z. M. Wei, H. P. Zhou and Q. Chen, *Science*, 2022, **378**, 747–754.
11 M. L. Li, M. Liu, F. Qi, F. R. Lin and A. K. Y. Jen, *Chem. Rev.*, 2024, **124**, 2138–2204.
12 Y. Zhao, F. Ma, Z. H. Qu, S. Q. Yu, T. Shen, H. X. Deng, X. B. Chu, X. X. Peng, Y. B. Yuan, X. W. Zhang and J. B. You, *Science*, 2022, **377**, 531–534.
13 S. Zhang, F. Y. Ye, X. Y. Wang, R. Chen, H. D. Zhang, L. Q. Zhan, X. Y. Jiang, Y. W. Li, X. Y. Ji, S. J. Liu, M. J. Yu, F. R. Yu, Y. L. Zhang, R. H. Wu, Z. H. Liu, Z. J. Ning, D. Neher, L. Y. Han, Y. Z. Lin, H. Tian, W. Chen, M. Stolterfoht, L. J. Zhang, W. H. Zhu and Y. Z. Wu, *Science*, 2023, **380**, 404–409.
14 Q. Fu, X. Tang, H. Liu, R. Wang, T. Liu, Z. Wu, H. Y. Woo, T. Zhou, X. Wan, Y. Chen and Y. Liu, *J. Am. Chem. Soc.*, 2022, **144**, 9500–9509.
15 J. Chen, Y. Zhou, Y. P. Fu, J. Pan, O. F. Mohammed and O. M. Bakr, *Chem. Rev.*, 2021, **121**, 12112–12180.
16 T. Zhou, Z. Y. Xu, R. Wang, X. Y. Dong, Q. Fu and Y. S. Liu, *Adv. Mater.*, 2022, **34**, 2200705.
17 A. B. Yusoff, M. Vasilopoulou, D. G. Georgiadou, L. C. Palilis, A. Abate and M. K. Nazeeruddin, *Energy Environ. Sci.*, 2021, **14**, 2906–2953.
18 Z. L. Song, Y. P. Gao, Y. Zou, H. Zhang, R. Wang, Y. Chen, Y. S. Chen and Y. S. Liu, *J. Am. Chem. Soc.*, 2024, **146**, 1657–1666.
19 Q. Jiang, Y. Zhao, X. W. Zhang, X. L. Yang, Y. Chen, Z. M. Chu, Q. F. Ye, X. X. Li, Z. G. Yin and J. B. You, *Nat. Photonics*, 2019, **13**, 460–466.
20 J. R. Wang, L. Y. Bi, X. F. Huang, Q. F. Feng, M. Liu, M. Q. Chen, Y. D. An, W. L. Jiang, F. R. Lin, Q. Fu and A. K. Y. Jen, *eScience*, 2024, **4**, 100308.
21 C. Luo, G. H. J. Zheng, F. Gao, X. J. Wang, C. L. Zhan, X. Y. Gao and Q. Zhao, *Nat. Photonics*, 2023, **17**, 856–964.
22 F. H. Isikgor, S. Zhumagali, L. V. T. Merino, M. De Bastiani, I. McCulloch and S. De Wolf, *Nat. Rev. Mater.*, 2023, **8**, 89–108.
23 Y. Yang, H. Chen, C. Liu, J. Xu, C. Y. Huang, C. D. Malliakas, H. Y. Wan, A. S. R. Bati, Z. W. Wang, R. P. Reynolds, I. W. Gilley, S. Kitade, T. E. Wiggins, S. Zeiske, S. Suragtkhuu, M. Batmunkh, L. X. Chen, B. Chen, M. G. Kanatzidis and E. H. Sargent, *Science*, 2024, **386**, 898–902.
24 R. Azmi, D. S. Utomo, B. Vishal, S. Zhumagali, P. Dally, A. M. Risqi, A. Prasetio, E. Ugur, F. F. Cao, I. F. Imran, A. A. Said, A. R. Pininti, A. S. Subbiah, E. Aydin, C. X. Xiao, S. I. Seok and S. De Wolf, *Nature*, 2024, **628**, 93–98.
25 Y. Zou, Y. P. Gao and Y. S. Liu, *Mater. Chem. Front.*, 2024, **8**, 82–103.
26 I. Metcalf, S. Sidhik, H. Zhang, A. Agrawal, J. Persaud, J. Hou, J. Even and A. D. Mohite, *Chem. Rev.*, 2023, **123**, 9565–9652.
27 Y. R. Wang, R. X. Lin, C. S. Y. Liu, X. Y. Wang, C. Chosy, Y. Haruta, A. D. Bui, M. H. Li, H. F. Sun, X. T. Zheng, H. W. Luo, P. Wu, H. Gao, W. J. Sun, Y. F. Nie, H. S. Zhu, K. Zhou, H. T. Nguyen, X. Luo, L. D. Li, C. X. Xiao, M. I. Saidaminov, S. D. Stranks, L. J. Zhang and H. R. Tan, *Nature*, 2024, **635**, 867–873.
28 T. Zhou, H. T. Lai, T. T. Liu, D. Lu, X. J. Wan, X. D. Zhang, Y. S. Liu and Y. S. Chen, *Adv. Mater.*, 2019, **31**, 1901242.
29 Y. Zhong, G. L. Liu, Y. Su, W. P. Sheng, L. Y. Gong, J. Q. Zhang, L. C. Tan and Y. W. Chen, *Angew. Chem., Int. Ed.*, 2022, **61**, e202114588.
30 R. Azmi, D. S. Utomo, B. Vishal, S. Zhumagali, P. Dally, A. M. Muhammad Risqi, A. Prasetio, E. Ugur, F. Cao, I. F. Imran, A. A. Ali Said, A. R. Pininti, A. S. Subbiah, E. Aydin, C. Xiao, S. I. Seok and S. D. De Wolf, *Nature*, 2024, **628**, 93–98.
31 Z. J. Shi, S. C. Liu, R. Luo, J. P. Ma, H. Tian, X. Wang, Z. J. Dong, X. Guo, J. X. Chen, J. A. Feng, C. X. Xiao, Y. C. Wu, W. P. Hu and Y. Hou, *J. Am. Chem. Soc.*, 2024, **147**, 1055–1062.
32 H. Y. Li, C. Zhang, C. Gong, D. L. Zhang, H. Zhang, Q. X. Zhuang, X. M. Yu, S. K. Gong, X. H. Chen, J. B. Yang, X. H. Li, R. Li, J. W. Li, J. F. Zhou, H. Yang, Q. Q. Lin, J. H. Chu, M. Grätzel, J. Z. Chen and Z. G. Zang, *Nat. Energy*, 2023, **8**, 946–955.
33 S. W. Liu, J. B. Li, W. S. Xiao, R. Chen, Z. X. Sun, Y. Zhang, X. Lei, S. F. Hu, M. Kober-Czerny, J. N. Wang, F. M. Ren, Q. S. Zhou, H. Raza, Y. Gao, Y. T. Ji, S. B. Li, H. Li, L. B. Qiu, W. C. Huang, Y. Zhao, B. M. Xu, Z. H. Liu, H. J. Snaith, N. G. Park and W. Chen, *Nature*, 2024, **632**, 536–542.

34 X. Yang, D. Luo, Y. Xiang, L. Zhao, M. Anaya, Y. Shen, J. Wu, W. Yang, Y. H. Chiang, Y. Tu, R. Su, Q. Hu, H. Yu, G. Shao, W. Huang, T. P. Russell, Q. Gong, S. D. Stranks, W. Zhang and R. Zhu, *Adv. Mater.*, 2021, **33**, e2006435.
35 X. Wang, J. Li, R. J. Guo, X. X. Yin, R. Luo, D. Y. Guo, K. Y. Ji, L. J. Dai, H. M. Liang, X. K. Jia, J. X. Chen, Z. R. Jia, Z. J. Shi, S. C. Liu, Y. D. Wang, Q. L. Zhou, T. Wang, G. J. Pan, P. Müller-Buschbaum, S. D. Stranks and Y. Hou, *Nat. Photonics*, 2024, **18**, 1269–1275.
36 R. Wang, X. Y. Dong, Q. Ling, Q. Fu, Z. Y. Hu, Z. Y. Xu, H. Zhang, Q. H. Li and Y. S. Liu, *ACS Energy Lett.*, 2022, **7**, 3656–3665.
37 B. Ding, Y. Ding, J. Peng, J. Romano-deGea, L. E. K. Frederiksen, H. Kanda, O. A. Syzgantseva, M. A. Syzgantseva, J. N. Audinot, J. Bour, S. Zhang, T. Wirtz, Z. F. Fei, P. Doerflinger, N. Shibayama, Y. J. Niu, S. X. Hu, S. L. Zhang, F. F. Tirani, Y. Liu, G. J. Yang, K. Brooks, L. H. Hu, S. Kinge, V. Dyakonov, X. H. Zhang, S. Y. Dai, P. J. Dyson and M. K. Nazeeruddin, *Nature*, 2024, **628**, 299–305.
38 M. Q. Tao, Y. Wang, K. Zhang, Z. F. Song, Y. J. Lan, H. D. Guo, L. T. Guo, X. W. Zhang, J. F. Wei, D. Q. Cao and Y. L. Song, *Joule*, 2024, **8**, 3142–3152.
39 N. Rolston, K. A. Bush, A. D. Printz, A. Gold-Parker, Y. C. Ding, M. F. Toney, M. D. McGehee and R. H. Dauskardt, *Adv. Energy Mater.*, 2018, **8**, 1802139.
40 J. H. Wu, Y. Q. Cui, B. C. Yu, K. Liu, Y. M. Li, H. S. Li, J. J. Shi, H. J. Wu, Y. H. Luo, D. M. Li and Q. B. Meng, *Adv. Funct. Mater.*, 2019, **29**, 1905336.
41 D. J. Xue, Y. Hou, S. C. Liu, M. Y. Wei, B. Chen, Z. R. Huang, Z. B. Li, B. Sun, A. H. Proppe, Y. T. Dong, M. I. Saidaminov, S. O. Kelley, J. S. Hu and E. H. Sargent, *Nat. Commun.*, 2020, **11**, 1514.
42 R. Wang, X. Y. Dong, Q. Ling, Z. Y. Hu, Y. P. Gao, Y. Chen and Y. S. Liu, *Angew. Chem., Int. Ed.*, 2023, **62**, e202314690.
43 D. Gebauer, M. Kellermeier, J. D. Gale, L. Bergstrom and H. Colfen, *Chem. Soc. Rev.*, 2014, **43**, 2348–2371.
44 Z. Xu, D. Lu, X. Dong, M. Chen, Q. Fu and Y. Liu, *Adv. Mater.*, 2021, **33**, 2105083.
45 G. X. Li, Y. L. Hu, M. Li, Y. Tang, Z. H. Zhang, A. Musiienko, Q. Cao, F. Akhundova, J. Z. Li, K. Prashanthan, F. J. Yang, P. Janasik, A. N. S. Appiah, S. Trofimov, N. Livakas, S. N. Zuo, L. Y. Wu, L. Y. Wang, Y. Q. Yang, B. Agyei-Tuffour, R. W. MacQueen, B. Naydenov, T. Unold, E. Unger, E. Aktas, S. Eigler and A. Abate, *Angew. Chem., Int. Ed.*, 2023, **62**, e202307395.
46 R. Azmi, E. Ugur, A. Seitkhan, F. Aljamaan, A. S. Subbiah, J. Liu, G. T. Harrison, M. Nugraha, M. K. Eswaran, M. Babics, Y. Chen, F. Z. Xu, T. G. Allen, A. U. Rehman, C. L. Wang, T. D. Anthopoulos, U. Schwingenschlögl, M. De Bastiani, E. Aydin and S. De Wolf, *Science*, 2022, **376**, 73–77.
47 O. Almora, C. Aranda, E. Mas-Marza and G. Garcia-Belmonte, *Appl. Phys. Lett.*, 2016, **109**, 173903.
48 J. H. Guo, B. Z. Wang, D. Lu, T. Wang, T. T. Liu, R. Wang, X. Y. Dong, T. Zhou, N. Zheng, Q. Fu, Z. Q. Xie, X. J. Wan, G. C. Xing, Y. S. Chen and Y. S. Liu, *Adv. Mater.*, 2023, **35**, 2212126.
49 T. Singh and T. Miyasaka, *Adv. Energy Mater.*, 2018, **8**, 1700677.